

# Silicon vacancy containing two hydrogen atoms studied with electron paramagnetic resonance and infrared absorption spectroscopy

P. Johannesen, R. Jakobsen, P. Stallinga, and B. Bech Nielsen\*  
*Institute of Physics and Astronomy, University of Aarhus, DK-8000 Århus C, Denmark*

J. R. Byberg  
*Institute of Chemistry, University of Aarhus, DK-8000 Århus C, Denmark*

(Received 5 July 2002; published 5 December 2002)

Float-zone and Czochralski-grown silicon crystals have been implanted with protons or deuterons. Electron-paramagnetic-resonance measurements performed during illumination with light at 1064 nm reveal a signal, labeled *DK5*, in addition to the well-known signal from  $\text{VO}^*$ —the excited spin-triplet state of the oxygen-vacancy defect. The *DK5* signal originates from a spin-triplet state of a vacancy-type defect with monoclinic-*I* (near-orthorhombic-*I*) symmetry. In contrast to the  $\text{VO}^*$  signal, *DK5* has about the same intensity in the spectra recorded on oxygen-lean and oxygen-rich samples, which indicates that the *DK5* defect is not oxygen related. However, the close resemblance between the *D* tensors of *DK5* and  $\text{VO}^*$  strongly suggests that the electron-spin distributions are similar in the two defects. Moreover, anisotropic hyperfine splittings from two proton spins are partially resolved in the *DK5* signal. The signal is assigned to  $\text{VH}_2^*$ , the excited spin-triplet state of the silicon vacancy containing two hydrogen atoms, which is the simplest defect consistent with the observed properties. The isochronal annealing behavior of *DK5* coincides with that of two infrared-absorption lines at 2063 and 2077  $\text{cm}^{-1}$ , which, like *DK5*, are observable only during illumination. These lines are assigned to Si-H stretch modes of  $\text{VH}_2^*$ .

DOI: 10.1103/PhysRevB.66.235201

PACS number(s): 61.72.Tt, 71.55.-i, 76.30.Mi

## I. INTRODUCTION

As the dimensions of the basic microelectronic components continue to shrink, there are good reasons to believe that the control of point defects residing in the bulk of crystalline silicon and at the silicon/silicon-dioxide interface will become even more important. The properties of point defects in silicon are strongly affected by the presence of hydrogen atoms in the material, mainly because hydrogen atoms bind strongly to such defects and thereby change their stability and electrical activity.<sup>1-3</sup> A detailed understanding of how the defect properties are modified requires identification of the atomic structure of the hydrogen defect. Hence, a rational exploitation of hydrogen-related processing of future devices may rely on structural information of hydrogen defects.

In this paper we focus on monovacancy-hydrogen defects  $\text{VH}_n$  ( $n = 1-4$ ) produced by proton implantation into silicon crystals.<sup>4-6</sup> Owing to the high level of radiation damage caused by the implantation, these defects are formed in relatively large quantities, making such samples suitable for structural studies.

The electronic properties of vacancy-type defects are commonly described in terms of “dangling bonds.” The creation of a vacancy is imagined as a sudden removal of a silicon atom, leaving each of its four silicon neighbors with a “dangling” or broken bond, i.e., with a singly occupied  $3sp^3$ -hybridized orbital pointing towards the site of the missing atom. The one-electron energy levels associated with these dangling-bond orbitals are taken to lie close to the middle of the silicon band gap. By the subsequent, inward distortion of the lattice, the silicon neighbors to the vacancy approach each other sufficiently to allow a moderately strong overlap of the dangling-bond orbitals. Some of the energy

levels corresponding to the resultant bonding and antibonding combinations lie *within* the band gap, which account for the electrical activity of the defect. In the neutral charge state, the bonding combinations become doubly occupied whereas the antibonding combinations are empty. Hence, the overlapping dangling bonds constitute weak elongated Si-Si bonds across the vacancy.

The binding energy of a Si-H bond is  $\sim 3.3$  eV, whereas the binding energy associated with the elongated Si-Si bonds is of the order 1 eV (Ref. 7). Therefore, a hydrogen atom added to the monovacancy will bind very strongly to one silicon atom, thereby eliminating one of the dangling bonds. Due to the strong binding, the Si-H unit is not associated with any one-electron states within the band gap and it is therefore electronically inert in this context. Thus, the electronic structure of this defect,  $\text{VH}$ , is determined primarily by the three remaining dangling bonds of which two form an elongated Si-Si bond while the last is unengaged. In the neutral charge state ( $\text{VH}^0$ ), the defect is paramagnetic and may be studied by electron-paramagnetic-resonance (EPR) spectroscopy.<sup>6</sup> In the ground state, the unpaired electron-spin density is largely confined to the “free” dangling bond, and the electronic structure is very similar to that of the well-known *E* center ( $\text{VP}^0$ ) (Ref. 8), in which the Si-H unit of  $\text{VH}^0$  is replaced by a phosphorus atom. By the same token, the electronic properties of  $\text{VH}_2$  may be expected to resemble those of the *A* center ( $\text{VO}$ ) (Ref. 9), since in both defects *two* dangling bonds have been eliminated: In the *A* center, the oxygen atom is strongly bonded to two silicon atoms, whereas two strong Si-H bonds are formed in  $\text{VH}_2$ .

Like the neutral *A* center,  $\text{VH}_2^0$  should be diamagnetic in the electronic ground state and, hence, unobservable by EPR.

However, the  $A$  center has an excited spin-triplet state ( $S = 1$ ) corresponding to the transfer of an electron from the bonding to the antibonding combination of the two dangling bonds.<sup>10</sup> This state, denoted  $VO^*$ , can be populated by optical excitation, and it is sufficiently long lived to allow detection by EPR under continuous illumination with band-edge light. The assumed similarity of the two defects suggests that  $VH_2^0$  could also be EPR-active under illumination.

Previously, Chen *et al.*<sup>11</sup> reported on an optically detected magnetic-resonance (ODMR) signal from an excited  $S = 1$  state of a defect with  $C_{2v}$  symmetry, which was observed in Czochralski-grown (oxygen-rich) silicon that had been exposed to a hydrogen or deuterium plasma and subsequently irradiated with 2-MeV electrons at room temperature. Two sets of satellite lines associated with hyperfine interaction were partly resolved. From a comparison between spectra recorded on hydrogen- and deuterium-treated samples, it was argued that the signal originates from a defect containing two equivalent hydrogen atoms. From this and the magnitude of the components of the derived  $D$  tensor, the signal was assigned to  $VH_2^*$ , the excited  $S = 1$  state of  $VH_2^0$ . In a later comment<sup>12</sup> it was noted that the line positions derived from the spin Hamiltonian presented by Chen *et al.*<sup>11,13</sup> coincide with those of the  $VO^*$  signal within experimental error.

In the present study, the effect of band-edge illumination on proton- and deuteron-implanted silicon crystals grown either by the float-zone or the Czochralski technique has been investigated. A new light-induced EPR signal, denoted  $DK5$ , arising from a defect in a photoexcited spin-triplet state ( $S = 1$ ), has been detected. The properties derived for the defect giving rise to  $DK5$  are similar to, but clearly distinct from, those of  $VO^*$  as well as those corresponding to the ODMR signal discussed above and are shown to be consistent with those expected for  $VH_2^*$ . Parallel EPR and Fourier-transform infrared (FTIR) measurements on similar samples indicate that  $VH_2^*$  possesses Si-H stretch modes at 2063.1 and 2077.4  $\text{cm}^{-1}$ .

## II. EXPERIMENTAL DETAILS

### A. Sample preparation

Samples for the EPR measurements shaped as rectangular parallelepipeds with dimensions  $0.6 \times 4 \times 15 \text{ mm}^3$  were cut from float-zone (FZ) and Czochralski-grown (CZ) silicon crystals. The large faces were perpendicular to the  $[111]$  axis and the small faces ( $0.6 \times 4 \text{ mm}^2$ ) perpendicular to the  $[1\bar{1}0]$  axis. The oxygen contents of the FZ and CZ samples were  $< 5 \times 10^{15}$  and  $\sim 6 \times 10^{17} \text{ cm}^{-3}$ , respectively, whereas the concentration of carbon was below  $5 \times 10^{15} \text{ cm}^{-3}$  in both types of samples. The FZ material was  $n$  type with resistivity  $\sim 600 \text{ } \Omega \text{ cm}$ , corresponding to a phosphorus concentration of  $\sim 9 \times 10^{12} \text{ cm}^{-3}$ , and the CZ material was  $p$  type with resistivity  $\sim 12 \text{ } \Omega \text{ cm}$ , equivalent to a boron concentration of  $\sim 1 \times 10^{15} \text{ cm}^{-3}$ . The samples were implanted with protons or deuterons through a 0.2-mm aluminum foil into the  $4 \times 15\text{-mm}^2$  faces at a sequence of energies ranging from 5.0 to 10.6 MeV. The implanted dose at each energy was adjusted to ensure a uniform distribution of hydrogen isotopes

throughout the sample corresponding to a concentration of  $(3.3 \pm 0.4) \times 10^{17} \text{ cm}^{-3}$ . During the implantation, the sample temperature was kept below 110 K with an average of  $\sim 50$  K. After the implantation, the samples were heated slowly to room temperature and etched lightly in nitric and hydrofluoric acids to remove surface defects that might be paramagnetic. In the following, samples implanted with protons and deuterons will be denoted Si:H and Si:D, respectively.

A similar FZ-Si:H sample was used for the FTIR measurements. This sample, measuring  $4 \times 10 \times 10 \text{ mm}^3$ , was cut from the same material as the FZ samples for EPR measurements. It was implanted with protons through a 0.2-mm aluminum foil into one of the large faces at 35 successive energies ranging from 9.4 to 5.1 MeV. The doses at each energy were adjusted to produce a 0.41-mm-thick layer in the sample with a uniform hydrogen concentration of  $(9.8 \pm 1.2) \times 10^{17} \text{ cm}^{-3}$ . The temperature of the sample was kept below 200 K during the implantation with an average of  $\sim 50$  K. After the implantation, the sample was allowed to warm to room temperature.

The local concentration of hydrogen is about three times higher in the FTIR samples than in the EPR samples. Previous FTIR experiments have shown that the higher concentration leads to larger intensity of the relevant FTIR lines without significant broadening of the lines. The width of EPR lines are, however, more sensitive to the strain caused by implantation damage, which justifies the choice of a lower concentration in that case.

### B. EPR measurements

The EPR spectra were recorded with a Bruker ESP300E spectrometer operated at  $X$  band ( $\sim 9.2 \text{ GHz}$ ) in the absorption mode. Conventional field modulation with synchronous lockin detection at 100 kHz was employed. The microwave frequency  $\nu_0$  and the static magnetic field  $\mathbf{B}_0$  were monitored continuously during the measurements with a Hewlett-Packard 5350B frequency counter and a Bruker ER035M nuclear magnetic resonance gaussmeter. Using epoxy resin, the sample was glued to a silver rod, which was screwed into the cold block of an Air Products and Chemicals LT-3-110 liquid-helium flow cryostat. The silver rod was thermally shielded by means of a thin-walled, silvered brass tube, and a quartz tube surrounding the sample served as a vacuum shroud. The temperature of the cold block was monitored and could be controlled in the range 5–300 K. The dimension of the quartz tube allowed the sample to be placed in the center of a Varian V-4533 cylindrical room-temperature cavity. The magnet could be rotated in a horizontal plane, which, together with the fact that the cryostat-cavity assembly could be tilted several degrees in the vertical plane containing  $\mathbf{B}_0$ , allowed us to align  $\mathbf{B}_0$  with any direction in the  $(1\bar{1}0)$  plane of the sample. Moreover, because of the presence of the well-known, strongly anisotropic signal from  $VO^*$  (Ref. 10),  $\mathbf{B}_0$  could be aligned with any of the main axes  $[001]$ ,  $[111]$ , and  $[110]$ , to within  $0.05^\circ$ .

During measurements, the sample could be illuminated with light at 1064 nm from a continuous-wave Nd:YAG laser. The light was passed through an optical fiber, one end of

which fitted into a small hole in the cavity. The intensity of light incident on the sample was kept constant at about  $0.2 \text{ W/cm}^2$ , because this value optimized the spectral intensity of the *DK5* signal discussed below. Illumination at this intensity on samples with identical dimensions and the same mounting lead to sample temperatures  $15 \pm 5 \text{ K}$  higher than that of the cold block. In the absence of illumination the sample temperature exceeded the cold block temperature by  $3 \pm 2 \text{ K}$ . The sample temperatures stated below were determined from the block temperature and the relevant temperature difference.

### C. Annealing study and FTIR measurements

Infrared-absorption measurements were performed with a Nicolet, System 800, Fourier-transform spectrometer equipped with a glowbar source, a Ge:KBr beam splitter, and a mercury-cadmium-telluride detector. The sample was mounted in a closed-cycle helium cryostat with CsI windows. Measurements were performed at  $10 \text{ K}$  with an apodized resolution of  $0.6 \text{ cm}^{-1}$ . The sample could be illuminated with light from an external tungsten-halogen lamp through a quartz light guide, which resulted in a wide spectrum covering the range from  $\sim 4500$  to  $11\,000 \text{ cm}^{-1}$ . A low-pass filter with cutoff at  $2200 \text{ cm}^{-1}$  was placed in front of the internal glowbar source, and the effect of the light from the external lamp was investigated as follows: The sample was first illuminated continuously for  $70 \text{ min}$  at  $10 \text{ K}$ . Then the external lamp was switched off, and an interferogram was recorded for  $5 \text{ min}$ . Immediately after, the lamp was switched on again, and a similar interferogram was recorded. The measurements without and with external light were repeated several times and the results were reproducible. However, without the initial  $70\text{-min}$  illumination the results were irreproducible due to a light-induced intensity change with a time constant of  $\sim 20 \text{ min}$ .

EPR and FTIR spectra were recorded as described above after each step in a sequence of  $30\text{-}$  (EPR) or  $45\text{-min}$  (FTIR) heat treatments at temperatures in the range  $423\text{--}648 \text{ K}$ . The temperature increment was  $\sim 25\text{-K}$  per step. The heat treatments were performed in a tube furnace in ambient nitrogen. Only EPR lines that are insensitive to moderate misalignment of the sample were used to monitor the intensity of the EPR signal discussed below. The FTIR absorbance lines of interest were fitted with a Lorentzian line shape, and the intensities were determined from the areas under these curves.

## III. RESULTS

### A. EPR measurements

An EPR spectrum of FZ-Si:H recorded during band-edge illumination at  $20 \text{ K}$  with  $\mathbf{B}_0$  along the  $[001]$  axis, is shown in Fig. 1. The central lines lying within the field range  $319\text{--}332 \text{ mT}$ , most of which are off scale in the figure, are fully accounted for in terms of the  $\text{VH}^0$ ,  $S1_a$ , and  $S1_b$  signals, including  $^{29}\text{Si}$  hyperfine satellites.<sup>6,14</sup> The eight additional lines at positions outside this central region, which is characteristic for signals from defects with spin  $S=1/2$ , are ob-

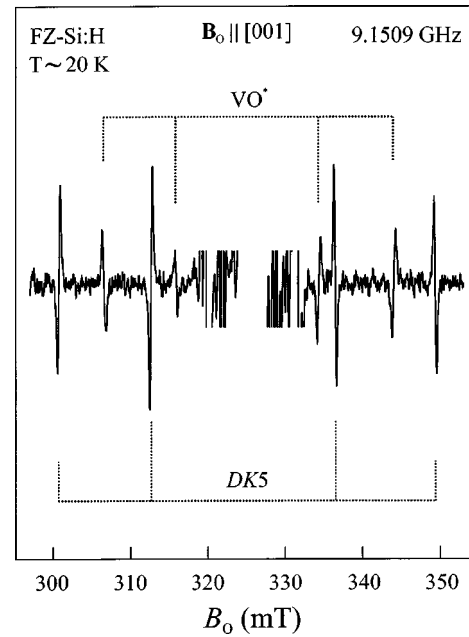


FIG. 1. Solid curve: EPR spectrum of a FZ-Si:H sample recorded during band-edge illumination at  $\sim 20 \text{ K}$  with  $\mathbf{B}_0$  along  $[001]$  and with a large modulation amplitude. The broken lines show the simulated resonant field values for  $\text{VO}^*$  and  $\text{DK5}$ , calculated from the  $g$  and  $D$  tensors listed in Table I. The central, very intense part of the observed spectrum has been cut out to accentuate the weak  $\text{VO}^*$  and  $\text{DK5}$  signals.

served only during illumination. Their integrated intensity is about 30-times smaller than that of the main lines from  $\text{VH}^0$ ,  $S1_a$ , and  $S1_b$ . In order to obtain a satisfactory signal-to-noise ratio for the weak light-induced lines, the spectrum was recorded with a large modulation amplitude at the expense of spectral resolution. The signal from  $\text{VO}^*$  accounts for four of the light-induced lines as indicated by the stick diagram in Fig. 2, which was calculated from the spin Hamiltonian

$$H = \mu_B \mathbf{S} \cdot \mathbf{g} \cdot \mathbf{B}_0 + \mathbf{S} \cdot \mathbf{D} \cdot \mathbf{S} \quad (1)$$

with  $S=1$  and the  $g$  and  $D$  tensors of  $\text{VO}^*$  with orthorhombic- $I$  symmetry found by Brower<sup>10</sup> (see Table I). The symbol  $\mu_B$  denotes the Bohr magneton. Each magnetically distinct orientation of  $\text{VO}^*$  has a pair of *fine-structure* transitions according to the selection rules  $M_S=0 \leftrightarrow M_S=\pm 1$ , where  $M_S$  is the quantum number for the component of the total spin along  $\mathbf{B}_0$  (the quantization axis). With  $\mathbf{B}_0$  parallel to the  $[001]$  axis, an orthorhombic- $I$  defect such as  $\text{VO}^*$  has just two magnetically distinct orientations, one with the  $C_2$  axis parallel to  $\mathbf{B}_0$  (twofold degenerate) and one with the  $C_2$  axis perpendicular to  $\mathbf{B}_0$  (fourfold degenerate), which yield the outer and inner pairs of lines in Fig. 1, respectively. The two  $\text{VO}^*$  lines to the left have the same sign as the central lines from  $S=1/2$  defects and therefore represent a net *absorption* of microwave power. However, the right-hand lines both have opposite sign (=negative), corresponding to a net *emission* of microwave power. This spectral feature, characteristic of excited states with  $S \geq 1$ , reflects that spin-

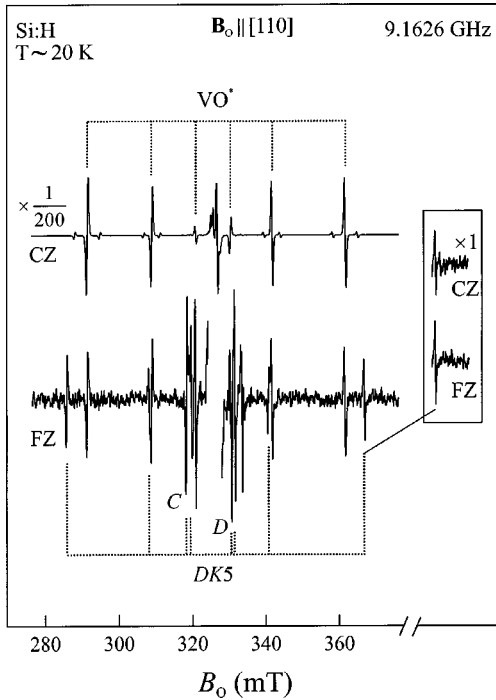


FIG. 2. Comparison of the EPR spectra of proton-implanted CZ and FZ samples recorded during band-edge illumination at  $\sim 20$  K with  $\mathbf{B}_0$  along  $[110]$  and with a large modulation amplitude. The CZ spectrum has been scaled with a factor of 0.005 to make the intensities of the  $\text{VO}^*$  lines similar in the two spectra. The broken lines represent the calculated line positions of  $\text{VO}^*$  and  $\text{DK5}$ . In the inset the outermost  $\text{DK5}$  line in the CZ and FZ spectra is plotted on the same vertical scale.

dependent excitation and deexcitation processes may create a population inversion among the magnetic sublevels. Moreover, as these processes depend strongly on the orientation of the defect with respect to  $\mathbf{B}_0$ , the relative amplitudes of the inner and outer pairs of lines deviate from the 2:1 ratio between the degeneracies of the corresponding orientations.

The four remaining light-induced lines in the spectrum belong to a signal which we label  $\text{DK5}$ . The  $\text{DK5}$  signal resembles the  $\text{VO}^*$  signal in the sense that it also consists of two line pairs along  $[001]$ , and has two positive and two negative lines. This suggests that the  $\text{DK5}$  signal also originates from a defect with  $S=1$  and orthorhombic- $I$  symmetry. The line positions of  $\text{DK5}$  may in fact be represented in terms of the spin Hamiltonian [Eq. (1)] with  $S=1$ . However, the remote possibility of a spin quartet state ( $S=\frac{3}{2}$ ) cannot be rigorously refuted.<sup>15</sup> The  $g$  and  $D$  tensors obtained from the best fit of Eq. (1) to all the data reveal that the symmetry of the  $\text{DK5}$  defect is monoclinic- $I$  rather than orthorhombic- $I$  (Table I), although a monoclinic term is noticeable only for the  $g$  tensor. The seven independent parameters of the monoclinic- $I$   $g$  and  $D$  tensors for  $\text{DK5}$  were obtained from the positions of 22 fine-structure lines that are not obscured by overlapping lines from other signals in the spectra recorded with  $\mathbf{B}_0$  along  $[001]$ ,  $[001]+30^\circ$ ,  $[111]$ ,  $[001]+73^\circ$ , and  $[110]$ , in the  $(1\bar{1}0)$  plane. A stick diagram calculated from the resultant parameters is included in Fig. 1.

As noted above, the  $\text{DK5}$  signal is observable only during

TABLE I. Spin-Hamiltonian parameters for the  $\text{DK5}$  and  $\text{VO}^*$  (Ref. 10) signals and for the  $\text{VH}_2^*$  signal as calculated from a biradical model (Sec. IV B). Principal values of  $\mathbf{D}$  and  $\mathbf{A}_{H,1}$  are given in MHz. The principal axis  $X'$  of  $\mathbf{g}$  and  $\mathbf{D}$  is parallel to the  $[1\bar{1}0]$  axis, while  $Y'$  and  $Z'$  span the  $(1\bar{1}0)$  plane.  $\Theta'$  denotes the angle between  $Y'$  and the  $[110]$  axis. The principal axis  $Y''$  of  $\mathbf{A}_{H,1}$  is parallel to the  $[110]$  axis, and the  $X''$  and  $Z''$  axes span the  $(110)$  plane.  $\Theta''$  denotes the angle between  $X''$  and the  $[1\bar{1}0]$  axis. Limits of error are given in brackets.

| Term               | Principal direction | $\text{DK5}$    | $\text{VO}^*$ | $\text{VH}_2^*$ (biradical model) |
|--------------------|---------------------|-----------------|---------------|-----------------------------------|
| $\mathbf{g}$       | $X'$                | 2.0140 (3)      | 2.0102 (1)    | 2.0114                            |
|                    | $Y'$                | 2.0062 (3)      | 2.0058 (1)    | 2.0030                            |
|                    | $Z'$                | 2.0089 (3)      | 2.0076 (1)    | 2.0066                            |
|                    | $\Theta' (^\circ)$  | 23 (2)          | 0             | 0                                 |
| $\mathbf{D}$       | $X'$                | $\pm 304.3$ (6) | 307.0 (2)     | 459                               |
|                    | $Y'$                | $\mp 758.7$ (6) | $-657.0$ (2)  | $-918$                            |
|                    | $Z'$                | $\pm 454.4$ (6) | 350.0 (2)     | 459                               |
|                    | $\Theta' (^\circ)$  | 0.6 (2)         | 0             | 0                                 |
| $\mathbf{A}_{H,1}$ | $X''$               |                 |               | $-4.1$                            |
|                    | $Y''$               |                 |               | 0.5                               |
|                    | $Z''$               |                 |               | 4.2                               |
|                    | $\Theta'' (^\circ)$ |                 |               | 32                                |

band-edge illumination: Switching the laser off during a scan results in the immediate disappearance of the signal. The  $\text{DK5}$  signal becomes unobservable at temperatures above  $\sim 100$  K, whereas the  $\text{VO}^*$  signal disappears above  $\sim 160$  K. Moreover, the  $\text{DK5}$  signal appears to be turned upside down with respect to the  $\text{VO}^*$  signal for  $\mathbf{B}_0$  along  $[001]$  so that the negative lines of  $\text{DK5}$  occur on the left-hand side of the central region for this direction.

Figure 2 shows the spectra of CZ- and FZ-Si:H recorded under the same conditions as the spectrum in Fig. 1 but with  $\mathbf{B}_0$  along the  $[110]$  axis. The stick diagrams represent the calculated resonant field values of  $\text{VO}^*$  and  $\text{DK5}$  for this direction. Since the CZ spectrum has been scaled down by a factor of 200, it appears from the figure that the intensity of the  $\text{VO}^*$  signal is about two orders-of-magnitude larger in the oxygen-rich sample than in the oxygen-lean sample. In contrast, the  $\text{DK5}$  signal has about the same intensity in both types of samples, as illustrated in the inset at the right-hand side of the figure. This fact by itself strongly suggests that the  $\text{DK5}$  defect is not related to oxygen.

The  $\text{DK5}$  lines at 318 and 331 mT, denoted  $C$  and  $D$  in Fig. 2, are of particular interest in the following. Small sections of the FZ-Si:H spectrum in Fig. 2, which display these lines, are shown in Fig. 3. Also shown in this figure are simulations of the lines originating from the  $\text{VH}^0$ ,  $S1$  ( $S1_a$  and  $S1_b$ ), and  $\text{VO}^*$  defects, and a simulation of the  $\text{DK5}$  lines. As can be seen from the figure the simulations account for the observed spectrum. Furthermore, it is evident that the  $C$  and  $D$  lines have only a minor overlap with other lines.

As mentioned above, the large modulation amplitude employed to record these spectra leads to broadening of the lines,<sup>16</sup> the resultant peak-to-peak width of the  $\text{DK5}$  lines

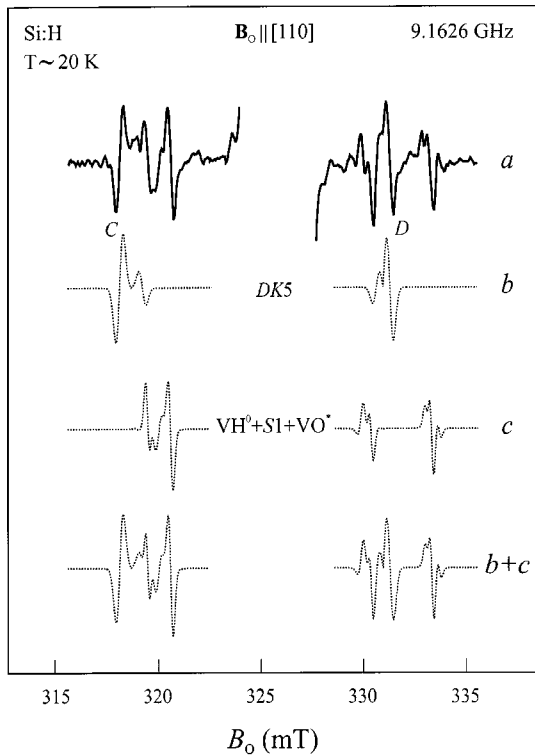


FIG. 3. Expanded view of sections around the lines marked *C* and *D* in the FZ-Si:H spectrum of Fig. 2 (curve *a*). Curve *b*: Simulated signal from *DK5*. Curve *c*: Simulated spectrum calculated from the spin Hamiltonian of  $S_{1a}$ ,  $S_{1b}$ , and  $VO^*$  (Refs. 10 and 14). The combined simulation  $b+c$  closely resembles the observed spectrum. Note that the lines *C* and *D* belong to *DK5* and, moreover, overlap only marginally with other lines.

being  $\sim 0.34$  mT, and under these conditions no differences between the line shapes in the spectra of Si:H and Si:D are observed. As the modulation amplitude is lowered, the widths of all the lines decrease. At the best obtainable resolution, most of the *DK5* lines in the spectra of Si:H resemble first-derivative Gaussian absorption lines with a peak-to-peak width of  $\sim 0.15$  mT. This is not the case, however, for line *C* and its partner line *D* belonging to the same orientation of the defect in the [110] spectrum (cf. Fig. 3). The line *C* in the spectra of FZ-Si:H and FZ-Si:D recorded at low modulation amplitude are shown as solid curves in Fig. 4. The spectra of Si:H and Si:D are clearly distinct: The line from Si:H is broader and has a more complex shape than that from Si:D. This indicates that hydrogen is involved in the *DK5* defect. Our data do not allow a derivation of the proton hyperfine tensor, but the observed shape of line *C* from Si:H is consistent with a hyperfine interaction of  $\sim 4$  MHz with *two* protons and is inconsistent with a hyperfine interaction with a single proton. The simulations included in Fig. 4 are based on hyperfine interaction with two protons and will be described further in Sec. IV B.

We have not detected any  $^{29}\text{Si}$  hyperfine satellites in the *DK5* signal, presumably because such lines are too weak to be detected with our spectrometer. The  $^{29}\text{Si}$  hyperfine satellites associated with the two equivalent silicon sites of  $VO^*$  are clearly visible in the CZ-Si:H spectrum shown in Fig. 2,

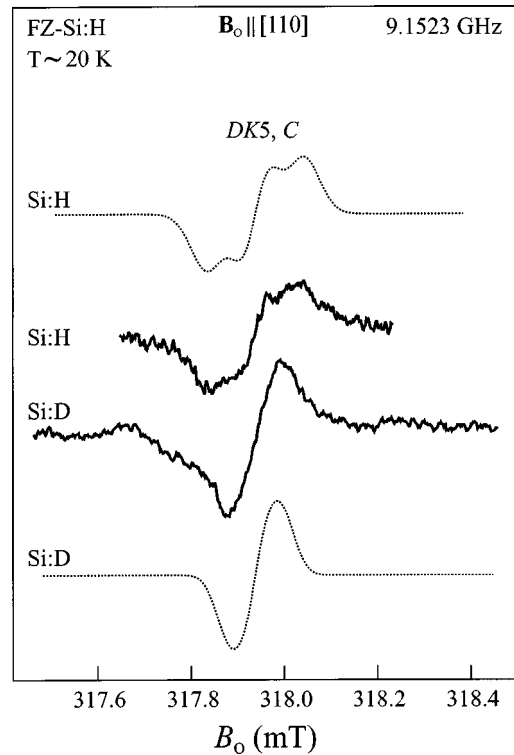


FIG. 4. Comparison of a section of the EPR spectra of FZ-Si:H and FZ-Si:D around the line *C* belonging to *DK5* (cf. Figs. 2 and 3). Solid curves are spectra recorded at  $\sim 20$  K during band-edge illumination with  $B_0$  along [110] and with a small modulation amplitude. The broken curves were calculated with the spin Hamiltonian derived from the biradical model of  $VH_2^*$  (see Sec. IV B).

curve *a*, but in the FZ-Si:H spectrum where the  $VO^*$  and *DK5* signals are about equally intense, the hyperfine satellites of  $VO^*$  fall below the detection limit.

## B. FTIR measurements and isochronal annealing

A section of the FTIR-absorbance spectrum recorded at 10 K without external illumination on the FZ-Si:H sample annealed at 548 K is shown as curve *a* in Fig. 5. The absorbance lines at  $2122.2$  and  $2145.0$   $\text{cm}^{-1}$  represent Si:H stretch modes of  $VH_2$ ,<sup>4,5</sup> and the lines at  $2068.1$  and  $2073.2$   $\text{cm}^{-1}$  are the stretch modes of  $V_2H^0$  and  $V_3H^0$  (or  $V_4H^0$ ), respectively.<sup>14</sup> The intense line at  $2072.4$   $\text{cm}^{-1}$  has recently been ascribed to  $V_2H_2$  (Refs. 17 and 18), and the weak lines in the range  $2078$ – $2088$   $\text{cm}^{-1}$  represent Si-H stretch modes of unidentified defects. When band-edge light is applied, new absorbance lines appear in the spectrum at  $2063.1$  and  $2077.4$   $\text{cm}^{-1}$  together with a weak line, denoted *X*, as can be seen from curve *b* in the figure. This spectrum was obtained by subtraction of the spectrum recorded without illumination from that recorded during band-edge illumination. When the external illumination is switched off, the  $2063$ - and  $2077$ - $\text{cm}^{-1}$  lines disappear immediately—like the *DK5* signal—in contrast to the *X* line, which decays very slowly. Thereby, the  $2063$ - and  $2077$ - $\text{cm}^{-1}$  lines are candidates for identification with Si-H stretch modes of the *DK5* defect. To investigate this possibility, the normalized intensities of the

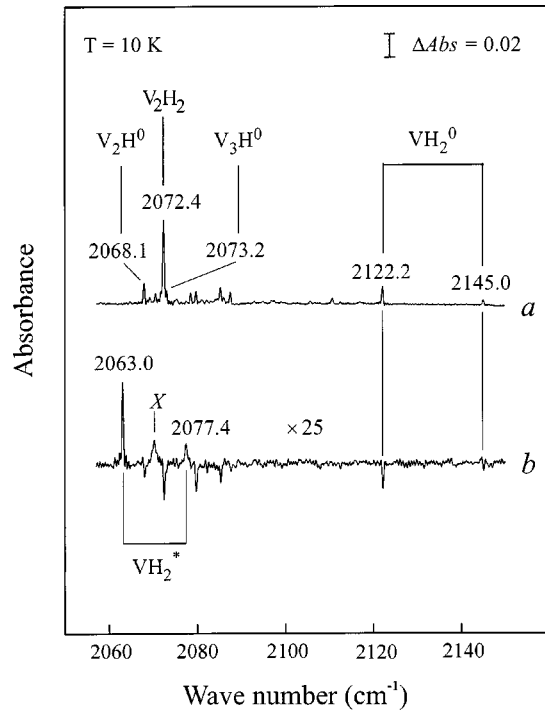


FIG. 5. Section of the FTIR-absorbance spectrum of FZ-Si:H covering the range of Si-H stretch modes of the vacancy-hydrogen defects. Curve *a*: Spectrum recorded at 10 K without band-edge illumination after annealing at 548 K. Curve *b*: Spectrum recorded at 10 K during band-edge illumination, from which the spectrum shown in curve *a* has been subtracted. The Si-H stretch modes ascribed to  $V_2H^0$ ,  $V_2H_2$ ,  $V_nH^0$  ( $n=3$  or  $4$ ), and  $VH_2$ , are indicated in curve *a* and those assigned here to  $VH_2^*$  are indicated in curve *b*.

*DK5* signal and the 2063- and 2077- $\text{cm}^{-1}$  lines are compared in Fig. 6. As can be seen from the figure, the annealing behavior of the *DK5* signal and the 2063- and 2077- $\text{cm}^{-1}$  lines are similar. The signal intensities increase with the annealing temperature up to  $\sim 590$  K, where the intensities are about four-times higher than observed in the as-prepared samples. When the annealing temperature is increased further, the signal intensities decay rapidly, and above  $\sim 650$  K the signals become unobservable. At annealing temperatures below 420 K the 2077- $\text{cm}^{-1}$  line appears to have a somewhat higher normalized intensity than the *DK5* signal and the 2063- $\text{cm}^{-1}$  line. However, the 2077- $\text{cm}^{-1}$  line is very weak in this temperature range and the apparent discrepancy falls well within the limits of error. Moreover, the *DK5* signal attains its maximum height after annealing at 548 K, whereas the 2063- and 2077- $\text{cm}^{-1}$  lines reach maximum intensity after annealing at 573 K. This slight shift is probably the result of a lower hydrogen concentration (a factor of 3) and a shorter annealing time (a factor of 1.5) for the EPR sample as compared with the FTIR sample. Hence, our measurements indicate that the annealing behaviors of the *DK5* signal and the 2063- and 2077- $\text{cm}^{-1}$  lines are in fact identical, and that the EPR signal and the two absorbance lines originate from the same defect. The described annealing behavior differs completely from that of any other EPR signal and FTIR ab-

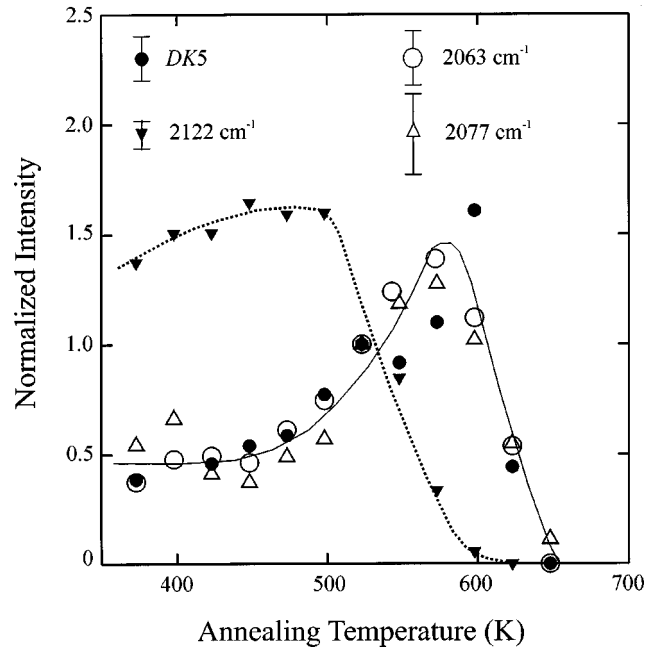


FIG. 6. Isochronal annealing curves for the EPR signal *DK5* and for the FTIR lines at 2063, 2077, and 2122  $\text{cm}^{-1}$ . The intensities of all signals have been normalized to the values obtained after annealing at 523 K. Within the limits of error, *DK5* and the lines at 2063 and 2077  $\text{cm}^{-1}$  grow in and decay in parallel.

sorbance line observed in our samples. Thus, there are no other absorbance lines that may be linked to the *DK5* signal.

The immediate appearance of the 2063- and 2077- $\text{cm}^{-1}$  lines caused by illumination is accompanied by a reduction of the intensities of the  $VH_2$  modes at 2122 and 2145  $\text{cm}^{-1}$  (see Fig. 5, curve *b*). Furthermore, the  $VH_2$  modes are immediately and fully restored while the 2063- and 2077- $\text{cm}^{-1}$  lines disappear when the light is switched off. This indicates that the 2063- and 2077- $\text{cm}^{-1}$  lines are somehow connected to  $VH_2$ . However, we note that the annealing behavior of the  $VH_2$  mode at 2122  $\text{cm}^{-1}$ , included in Fig. 5, differs from that of the 2063- and 2077- $\text{cm}^{-1}$  lines, even though they anneal out in the same temperature range as the  $VH_2$  mode.

## IV. DISCUSSION

### A. Assignments

The main experimental results obtained may be summarized as follows: The EPR signal *DK5* arises from a light-induced, excited state of a hydrogen-related defect, most probably in a spin-triplet state<sup>15</sup> ( $S=1$ ). Although the defect does not involve oxygen, the *DK5* signal is very similar to that of  $VO^*$ . This suggests that the *DK5* signal originates from  $VH_2^*$ ; the excited spin-triplet state of  $VH_2$  in its neutral charge state. Further evidence for this assignment comes from the infrared-absorbance spectrum which shows the presence of  $VH_2$  via the Si-H stretch modes at 2122 and 2145  $\text{cm}^{-1}$ . In addition, two new light-induced absorbance lines at 2063 and 2077  $\text{cm}^{-1}$  in the range characteristic of Si-H stretch modes exhibit the same unique annealing behavior as *DK5*. Reversible intensity changes of the 2122- and

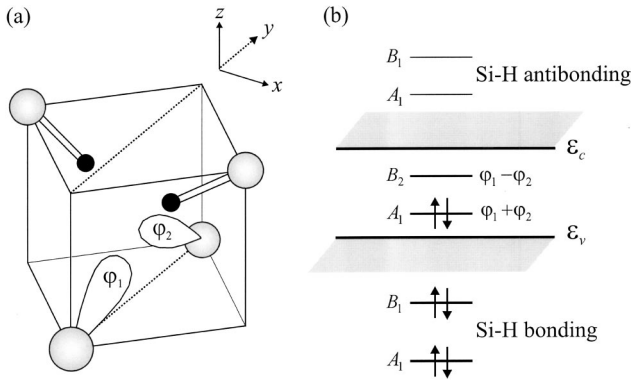


FIG. 7. (a) Model of the atomic structure of  $VH_2^0$ , showing the two hydrogen atoms (black) each bonded to a silicon atom adjacent to the vacancy. The dangling bonds  $\varphi_1$  and  $\varphi_2$  on the remaining two silicon neighbors form a long (reconstructed) bond in the  $(1\bar{1}0)$  mirror plane perpendicular to the one containing the Si-H bonds ( $x$  axis along  $[1\bar{1}0]$ ,  $y$  axis along  $[110]$ , and  $z$  axis  $[001]$ ). (b) Electronic structure of  $VH_2^0$ , as expected from a one-electron orbital treatment. The one-electron levels are labeled in accordance with the irreducible representations of the point group  $C_{2v}$  that describes the transformation properties of the corresponding orbitals.

$2145\text{-cm}^{-1}$  modes accompany the appearance and disappearance of these lines, which suggests that the lines originate from an excited electronic state of  $VH_2$ . On this basis, we assign the  $DK5$  signal to  $VH_2^*$  and ascribe the  $2063\text{-}$  and  $2077\text{-cm}^{-1}$  lines to Si-H stretch modes of the same defect.

### B. Biradical model

The expected orthorhombic- $I$  ( $C_{2v}$ ) structure of  $VH_2^0$  is sketched in Fig. 7. The structure of  $VH_2^*$  is expected to resemble that of  $VH_2^0$ . An ambiguity exists in the correlation of the observed spin Hamiltonian with the model of  $VH_2^*$ , since it cannot be determined experimentally whether the principal  $X'$  or  $Y'$  axis of the orthorhombic  $D$  tensor given in Table I is normal to the  $(110)$  plane containing the two dangling bonds. The choice made in Fig. 7 with the  $X'$  axis perpendicular to the dangling bonds is based on the comparison of the observed and expected  $g$  tensors, as explained below. As outlined above, the two dangling bonds  $\varphi_1$  and  $\varphi_2$  overlap and form bonding and antibonding combinations  $|a_1\rangle = 1/\sqrt{2} + 2S_{12}(\varphi_1 + \varphi_2)$  and  $|b_2\rangle = 1/\sqrt{2} - 2S_{12}(\varphi_1 - \varphi_2)$ , where  $S_{12}$  is the overlap integral  $S_{12} = \int \varphi_1^* \varphi_2 d\tau$ . In the ground state  $VH_2^0$ , the orbital  $|a_1\rangle$ , which belongs to the representation  $A_1$  of  $C_{2v}$ , is doubly occupied while  $|b_2\rangle$  belonging to  $B_2$  is empty, and the defect is diamagnetic. In accordance with the description of  $VO^*$ , we assume that the excitation of  $VH_2^0$  to  $VH_2^*$  implies the promotion of an electron from  $|a_1\rangle$  to  $|b_2\rangle$ , resulting in the triplet state  ${}^3B_2$ . This change virtually eliminates the bond between the silicon atoms carrying the orbitals  $\varphi_1$  and  $\varphi_2$ , and the distributions of electronic charge and spin therefore become similar to those of two independent dangling bonds, each holding one electron. Hence, the EPR spectrum may be interpreted in terms of a biradical consisting of two weakly interacting sub-

systems with  $S = \frac{1}{2}$ , where each electron spin interacts with both protons of the defect. Denoting by  $\mathbf{S}_1$  and  $\mathbf{S}_2$  the spin operators associated with the spin distributions of  $\varphi_1$  and  $\varphi_2$ , respectively, the spin Hamiltonian of the defect may therefore be written

$$H = \mu_B \mathbf{S}_1 \cdot \mathbf{g}_1 \cdot \mathbf{B}_0 + \mu_B \mathbf{S}_2 \cdot \mathbf{g}_2 \cdot \mathbf{B}_0 + 2\mathbf{S}_1 \cdot \mathbf{D} \cdot \mathbf{S}_2 + 2J\mathbf{S}_1 \cdot \mathbf{S}_2 + \sum_{j=1}^2 \mathbf{I}_{H,j} \cdot (\mathbf{A}_{H,j}^1 \cdot \mathbf{S}_1 + \mathbf{A}_{H,j}^2 \cdot \mathbf{S}_2 - g_H \mu_N \mathbf{B}_0), \quad (2)$$

where  $g_H$  and  $\mu_N$  denote the  $g$  factor of the proton and the nuclear magneton, respectively, and the tensors  $\mathbf{A}_{H,j}^1$  and  $\mathbf{A}_{H,j}^2$  describe the hyperfine interaction between the  $j$ th proton with nuclear spin  $\mathbf{I}_{H,j}$  and the electron spins  $\mathbf{S}_1$  and  $\mathbf{S}_2$ , respectively. The symbol  $J$  represents the exchange interaction between the electron spins. Owing to the assumed orthorhombic- $I$  symmetry, the two  $g$  tensors  $\mathbf{g}_1$  and  $\mathbf{g}_2$  are identical apart from the orientation of their principal axes. The same applies to the four-proton hyperfine tensors  $\mathbf{A}_{H,j}^1$  and  $\mathbf{A}_{H,j}^2$ . With the definitions

$$\mathbf{S} \equiv \mathbf{S}_1 + \mathbf{S}_2, \quad \Delta \mathbf{S} \equiv \mathbf{S}_1 - \mathbf{S}_2, \quad \Delta \mathbf{g} \equiv \mathbf{g}_1 - \mathbf{g}_2,$$

the spin Hamiltonian [Eq. (2)] can be expressed as

$$H = H^T + H', \quad (3a)$$

where

$$H^T = \frac{1}{2} \mu_B \mathbf{S} \cdot (\mathbf{g}_1 + \mathbf{g}_2) \cdot \mathbf{B}_0 + \mathbf{S} \cdot \mathbf{D} \cdot \mathbf{S} + J\mathbf{S} \cdot \mathbf{S} + \sum_{j=1}^2 \mathbf{I}_{H,j} \cdot \left[ \frac{1}{2} (\mathbf{A}_{H,j}^1 + \mathbf{A}_{H,j}^2) \cdot \mathbf{S} - g_H \mu_N \mathbf{B}_0 \right] \quad (3b)$$

and

$$H' = \frac{1}{2} \mu_B \Delta \mathbf{S} \cdot \Delta \mathbf{g} \cdot \mathbf{B}_0 + \frac{1}{2} \sum_{j=1}^2 \mathbf{I}_{H,j} \cdot (\mathbf{A}_{H,j}^1 - \mathbf{A}_{H,j}^2) \cdot \Delta \mathbf{S}. \quad (3c)$$

All terms in  $H^T$  commute with  $\mathbf{S}^2$ , and  $H^T$  has a triplet eigenstate ( $S=1$ ) and a singlet eigenstate ( $S=0$ ). The non-zero matrix elements of  $H'$  connect the singlet state with the substrates of the triplet.<sup>19</sup> Since the fine-structure lines of  $DK5$ , like those of  $VO^*$ , are well represented in terms of the triplet-spin Hamiltonian [Eq. (1)],  $H'$  is of little importance for this system in accordance with the expectation that the singlet-triplet energy separation is substantial compared to the matrix elements of  $H'$ . Hence, the EPR lines of  $VH_2^*$ , including the proton hyperfine splittings, are accurately represented by  $H^T$  alone. This part of the spin Hamiltonian may be expressed as

$$H^T = \mu_B \mathbf{S} \cdot \mathbf{g} \cdot \mathbf{B}_0 + \mathbf{S} \cdot \mathbf{D} \cdot \mathbf{S} + \sum_{j=1}^2 \mathbf{I}_{H,j} \cdot (\mathbf{A}_{H,j} \cdot \mathbf{S} - g_H \mu_N \mathbf{B}_0), \quad (4)$$

representing an  $S=1$  center containing two protons, with the  $g$  tensor  $\mathbf{g} = \frac{1}{2}(\mathbf{g}_1 + \mathbf{g}_2)$  and the two-proton hyperfine tensors

$\mathbf{A}_{H,j} = \frac{1}{2}(\mathbf{A}_{H,j}^1 + \mathbf{A}_{H,j}^2)$ . The term  $\mathbf{J}\mathbf{S}\cdot\mathbf{S}$  has been ignored here since it has no influence on the EPR spectrum. Observing that the relative position and orientation of a dangling bond and a Si-H unit in  $\text{VH}_2^*$  is about the same as in  $\text{VH}^0$  (Ref. 6), and, moreover, that  $\mathbf{g}_1$  and  $\mathbf{g}_2$  should each correspond to a “free” dangling bond in a vacancy as does  $\mathbf{g}(\text{VH}^0)$ , we may attempt to predict  $\mathbf{g}(\text{VH}_2^*)$  and  $\mathbf{A}_{H,j}(\text{VH}_2^*)$  by substituting  $\mathbf{g}_1$  and  $\mathbf{g}_2$  in Eq. (4) with  $\mathbf{g}(\text{VH}^0)$  (with the appropriate orientations), and, similarly, substituting  $\mathbf{A}_{H,j}^1$  and  $\mathbf{A}_{H,j}^2$  with  $\mathbf{A}_H(\text{VH}^0)$ . The result is given in the last column of Table I. As can be seen from the table, the calculated  $g$  tensor resembles the experimental tensor. In particular, we note that the ordering of calculated and observed  $g$  shifts is the same, from which we conclude that the  $X'$  axis of the (orthorhombic) spin Hamiltonian was correctly taken as the normal to the plane of the dangling bonds. The small monoclinic- $I$  component of  $\mathbf{g}(\text{VH}_2^*)$ , which evidently cannot be accounted for within the  $C_{2v}$  geometry assumed here, will be discussed in a separate subsection. (See Sec. IV D).

The hyperfine tensors  $\mathbf{A}_{H,1}$  and  $\mathbf{A}_{H,2}$  obtained from the biradical model were used in conjunction with the experimental  $g$  and  $D$  tensors (Table I) to calculate the proton hyperfine splittings expected for  $\text{VH}_2^*$ . The calculations show that for all orientations of  $\mathbf{B}_0$ , the splitting between the two outermost lines of each proton hyperfine quartet is smaller than or comparable to the observed peak-to-peak width of the  $DK5$  lines in the spectra recorded with a large modulation amplitude, in agreement with the lack of resolved proton hyperfine splittings in these spectra (Sec. III A). Moreover, the calculated hyperfine splittings of line  $C$  in the  $[110]$  spectrum are consistent with those observed, as may be seen from Fig. 4, in which simulations of line  $C$  in the spectra of Si:H and Si:D are included. The simulation of the Si:D spectrum has been obtained from Eq. (4) with the tensors  $\{\mathbf{A}_{H,j}\}$  multiplied by the ratio (0.154) between the nuclear  $g$  factors of the deuteron and the proton, and with the nuclear spin of the deuteron ( $I_D = 1$ ) replacing that of the proton. The calculated proton hyperfine splittings of the other fine-structure lines in the  $[110]$  spectrum are all smaller than or comparable to the observed peak-to-peak width of these lines recorded at the best obtainable resolution. This also applies to all the lines in the  $[001]$  spectrum, whereas the calculations suggest that one pair of fine-structure lines in the  $[111]$  spectrum has resolvable proton hyperfine splittings. However, the observed intensities of these lines are nearly zero, which precludes verification of this prediction. We may conclude that the proton hyperfine splittings of  $\text{VH}_2^*$  predicted from the biradical—or independent dangling-bond—model and  $\mathbf{A}_H(\text{VH}^0)$  account for the shape of the  $C$  line and for the observed differences between these lines from Si:H and Si:D. The proton hyperfine splittings are in general obliterated by the large inherent EPR linewidth of the photoexcited triplet state of  $\text{VH}_2^0$ .

### C. Interpretation of the $D$ tensor

With the orientation of the spin Hamiltonian relative to the model of  $\text{VH}_2^*$  derived from the  $g$  tensor, the largest principal value of the  $D$  tensor,  $D_{Y'}$ , is measured for  $\mathbf{B}_0$

parallel to the line connecting the atoms carrying the two dangling bonds  $\varphi_1$  and  $\varphi_2$ . This immediately suggests that the dominant contribution to  $\mathbf{D}$  arises from the magnetic dipole-dipole interaction between the spins. Indeed, if the spins are considered as classical dipoles, the tensor describing this interaction has the principal values  $D_{X'} = D_{Z'} = -\frac{1}{2}D_{Y'}$  with  $D_{Y'} = -g_e^2\mu_B^2R^{-3}$ , where  $g_e$  is the  $g$  factor of the free electron and  $R$  is the distance between the spins. Taking  $R$  equal to the nominal distance between the silicon nuclei carrying the dangling bonds in the model of Fig. 7 (3.84 Å in the unrelaxed lattice), we obtain  $D_{Y'} = -918$  MHz and  $D_{X'} = D_{Z'} = 459$  MHz in fair agreement with the experimental values of  $|D_{Y'}| = 758.7$ ,  $|D_{X'}| = 304.3$ , and  $|D_{Z'}| = 454.4$  MHz for  $DK5$ .

Before we declare this agreement a confirmation of the assignment of  $DK5$  to  $\text{VH}_2^*$ , other interactions that may contribute to  $\mathbf{D}$  must be briefly examined.<sup>20</sup> Such interactions are all related in some way to the spin-orbit coupling. Some of them, like the antisymmetric exchange,<sup>10,21</sup> produce antisymmetric contributions to  $\mathbf{D}$  and can therefore be ignored in this context, since the fine-structure splittings are fully accounted for in terms of a *symmetric*  $D$  tensor. However, other effects of the spin-orbit coupling may yield symmetric contributions to  $\mathbf{D}$ . The spin-orbit coupling operator may be expressed as<sup>22</sup>

$$H^{\text{SO}} = \sum_i \mathbf{R}_i \cdot \mathbf{S}_i \quad (5)$$

where the sum is taken over the electrons,  $\mathbf{S}_i$  is the electron spin, and the operator  $\mathbf{R}_i$  is

$$\mathbf{R}_i = -\frac{e\hbar}{2m_0c^2} \nabla\phi \times \mathbf{p}_i, \quad (6)$$

where  $e$  and  $m_0$  are the electron charge and mass,  $c$  is the velocity of light,  $\phi$  is the electrostatic potential, and  $\mathbf{p}_i$  is the momentum operator for the  $i$ th electron.  $H^{\text{SO}}$  is a sum of one-electron operators and, therefore, connects the ground state  $|G\rangle$  of  $\text{VH}_2^*$  only with those excited states that differ from the ground-state configuration by the promotion of a single electron to another (higher) orbital. Four types of such excited configurations occur, three of which may be conveniently discussed together: an electron may be transferred either from a doubly occupied orbital (state) in the valence band to a singly occupied orbital in the band gap or from a singly occupied orbital in the band gap to an empty orbital, normally in the conduction band. As the ground-state configuration in the present case has two singly occupied orbitals, so will both these types of excited configurations, thus giving rise to a spin-singlet and a spin-triplet state each. However, the third type of excited configuration, which arises by promoting an electron from a doubly occupied valence-band orbital to an empty conduction-band orbital, has *four* singly occupied orbitals and, hence, comprises 16 levels grouped as two singlets, three triplets, and one quintet state. The spin selection rules for matrix elements of  $H^{\text{SO}}$  are  $\Delta S = 0, \pm 1$  and  $\Delta M_S = 0, \pm 1$ , so that the ground-state triplet sublevels ( $M_S = 0, \pm 1$ ) may be shifted through coupling to

all these excited states (with the exception of one singlet). The substrates of  $|G\rangle$  with  $M_S = \pm 1$  and 0 couple to different excited (sub)states and may therefore be shifted differently, which could yield a contribution to the  $D$  tensor. However, it turns out that for each excited configuration  $|\Gamma\rangle$ , irrespective of the type of excitation, we find that

$$\sum_{s',M'_s} |\langle \Gamma S' M'_s | H^{SO} | G S M_S \rangle|^2 = \frac{1}{2} (|\langle \psi_\Gamma | R_{q_1} | \psi_G \rangle|^2 + |\langle \psi_\Gamma | R_{q_2} | \psi_G \rangle|^2 + |\langle \psi_\Gamma | R_{q_3} | \psi_G \rangle|^2), \quad (7)$$

where  $\psi_\Gamma$  and  $\psi_G$  are those orbitals in  $|\Gamma\rangle$  and  $|G\rangle$ , respectively, that make the two configurations different. The coordinates  $q_1$ ,  $q_2$ , and  $q_3$  refer to a system in which the  $q_3$  axis is chosen parallel to  $\mathbf{B}_0$ . Since the expression on the right-hand side of Eq. (7) is independent of  $M_S$ , so is the sum on the left-hand side. Therefore, if the ‘‘term splittings’’  $E_{\Gamma S'} - E_{\Gamma S''}$  are small compared to the electronic excitation energy  $E_\Gamma - E_G$ , then the shifts of the  $M_S = \pm 1$  and 0 sublevels of  $|G\rangle$ , as calculated by second-order perturbation theory, will be equal, and no contribution from coupling to excited configurations via  $H^{SO}$  will appear in the  $D$  tensor. The condition  $|E_{\Gamma S'} - E_{\Gamma S''}| \ll E_\Gamma - E_G$  is expected to be fulfilled in the present system, since  $E_\Gamma - E_G$  is of the order 1 eV, whereas  $|E_{\Gamma S'} - E_{\Gamma S''}|$  is probably less than  $10^{-2}$  eV, because the electrons are localized at different, well-separated centers.

We may note that the reversed inequality, an electronic excitation energy much smaller than the term splitting, is often seen for transition-metal ions in weak crystalline fields. In such cases only matrix elements of  $H^{SO}$  diagonal in  $S$  are important and, to second order in the spin-orbit coupling constant  $\xi$  of the  $L$ - $S$  term, the shifts of the ground-state levels produce a contribution  $\mathbf{D}^{(2)}$  to the  $D$  tensor that is proportional to the  $g$  shift  $\Delta\mathbf{g}$ .<sup>23</sup>

$$\mathbf{D}^{(2)} = -\frac{\xi}{2} \Delta\mathbf{g}. \quad (8)$$

It appears that this relationship may be validated by the presence of the very strong exchange-coupling characteristic of several unpaired electrons located on a single atomic ion, whereas its application to systems whose unpaired electrons are spread over several atoms is ill-advised, because matrix elements of  $H^{SO}$  that are off diagonal in  $S$  tend to cancel the effects of the matrix elements yielding  $\Delta\mathbf{g}$ .

While the foregoing discussion suggests that the first three types of excitation produce only negligible contributions to the  $D$  tensor, this does not necessarily apply to the fourth type of excitation discussed in the following. Here the excited configuration arises by transferring an electron from one of the two singly occupied orbitals of the ground-state configuration to the other. Two singlet states  $\mathbf{S}_0$  and  $\mathbf{S}_1$  result, with the corresponding wave functions  $\frac{1}{\sqrt{2}}|a_1 a_1\rangle(|\alpha\beta\rangle - |\beta\alpha\rangle)$  and  $\frac{1}{\sqrt{2}}|b_2 b_2\rangle(|\alpha\beta\rangle - |\beta\alpha\rangle)$ . These singlet states are coupled to the sublevels of the ground-state triplet  $\mathbf{T}_0$  by  $H^{SO}$ . The three wave functions of the triplet are  $\mathbf{T}_0^{+1} = \frac{1}{\sqrt{2}}|a_1 b_2 - b_2 a_1\rangle|\alpha\alpha\rangle$ ,  $\mathbf{T}_0^0 = \frac{1}{2}|a_1 b_2 - b_2 a_1\rangle(|\alpha\beta\rangle + |\beta\alpha\rangle)$ ,

and  $\mathbf{T}_0^{-1} = 1/\sqrt{2}|a_1 b_2 - b_2 a_1\rangle|\beta\beta\rangle$ . With the coordinates  $q_1$ ,  $q_2$ , and  $q_3$  defined above, the nonzero matrix elements of  $H^{SO}$  may be expressed as

$$|\langle \mathbf{T}_0^{\pm 1} | H^{SO} | \mathbf{S}_0 \rangle|^2 = |\langle \mathbf{T}_0^{\pm 1} | H^{SO} | \mathbf{S}_1 \rangle|^2 = \frac{1}{4} (|\langle a_1 | R_{q_1} | b_2 \rangle|^2 + |\langle a_1 | R_{q_2} | b_2 \rangle|^2), \quad (9)$$

$$|\langle \mathbf{T}_0^0 | H^{SO} | \mathbf{S}_0 \rangle|^2 = |\langle \mathbf{T}_0^0 | H^{SO} | \mathbf{S}_1 \rangle|^2 = \frac{1}{2} |\langle a_1 | R_{q_3} | b_2 \rangle|^2. \quad (10)$$

Hence, second-order perturbation theory yields the energy corrections:

$$E_{\mathbf{T}_0^{\pm 1}}^{(2)} = \frac{1}{4} (|\langle a_1 | R_{q_1} | b_2 \rangle|^2 + |\langle a_1 | R_{q_2} | b_2 \rangle|^2) \times \left( \frac{1}{E_{\mathbf{T}_0^{\pm 1}} - E_{\mathbf{S}_0}} + \frac{1}{E_{\mathbf{T}_0^{\pm 1}} - E_{\mathbf{S}_1}} \right), \quad (11)$$

where the Zeeman energy has been ignored in the denominators, and

$$E_{\mathbf{T}_0^0}^{(2)} = \frac{1}{2} |\langle a_1 | R_{q_3} | b_2 \rangle|^2 \left( \frac{1}{E_{\mathbf{T}_0^0} - E_{\mathbf{S}_0}} + \frac{1}{E_{\mathbf{T}_0^0} - E_{\mathbf{S}_1}} \right). \quad (12)$$

These energy corrections may give substantial symmetric contributions to the  $D$  tensor unless  $2E_{\mathbf{T}_0} \approx E_{\mathbf{S}_0} + E_{\mathbf{S}_1}$ , i.e., unless  $E_{\mathbf{S}_0}$  and  $E_{\mathbf{S}_1}$  are positioned symmetrically with respect to  $E_{\mathbf{T}_0}$  (taken as the mean value of  $E_{\mathbf{T}_0^{\pm 1}}$  and  $E_{\mathbf{T}_0^0}$ ).

To zeroth order,  $E_{\mathbf{S}_0}$ ,  $E_{\mathbf{T}_0}$ , and  $E_{\mathbf{S}_1}$  are indeed equidistant, with a separation equal to the one-electron excitation energy associated with the promotion of an electron from  $|a_1\rangle$  to  $|b_2\rangle$ . However, even a slight difference between  $E_{\mathbf{T}_0} - E_{\mathbf{S}_0}$  and  $E_{\mathbf{S}_1} - E_{\mathbf{T}_0}$  may yield a significant effect on  $E_{\mathbf{T}_0^{\pm 1}}$  and  $E_{\mathbf{T}_0^0}$  and hence also on  $\mathbf{D}$ .

If the magnetic field is along one of the  $C_{2v}$  ‘‘symmetry axes’’  $x$ ,  $y$ , or  $z$  shown in Fig. 7, the coordinates  $q_1$ ,  $q_2$ , and  $q_3$  may be chosen so that  $(q_1, q_2, q_3)$  is some permutation of  $(x, y, z)$ . From group theory the only nonzero matrix element of the type  $\langle a_1 | R_{q_j} | b_2 \rangle$  occurs for  $q_j = x$ . Hence  $E_{\mathbf{T}_0^0}^{(2)}$  vanishes for  $\mathbf{B}_0$  along the  $y$  or  $z$  axis, whereas  $E_{\mathbf{T}_0^{\pm 1}}^{(2)}$  vanishes for  $\mathbf{B}_0$  along the  $x$  axis, and the contribution to the  $D$  tensor is

$$\mathbf{D}^{(2)} = \frac{1}{6} |\langle a_1 | R_x | b_2 \rangle|^2 \left( \frac{1}{E_{\mathbf{T}_0} - E_{\mathbf{S}_0}} + \frac{1}{E_{\mathbf{T}_0} - E_{\mathbf{S}_1}} \right) \times \begin{pmatrix} -2 & 0 & 0 \\ 0 & 1 & 0 \\ 0 & 0 & 1 \end{pmatrix}. \quad (13)$$

We note that the axis of this axial tensor is directed along  $x$ , i.e., perpendicular to the plane of the two dangling bonds. Thus, the contribution given in Eq. (13) cannot be the domi-

nating term in the  $D$  tensor for the  $DK5$  defect, because the numerically largest principal value occurs along the  $y$  axis.

To sum up, we believe that the magnetic dipole-dipole coupling yields the dominant contribution to the observed  $D$  tensor in accordance with the direction of the axis of the largest principal value along  $Y'$ . However, a smaller component arising from coupling via  $H^{SO}$  to the singlet states  $S_0$  and  $S_1$  cannot be excluded; this component will be axial along the  $x$  axis in Fig. 7, and, with the reasonable assumption that  $E_{T_0} - E_{S_0} < E_{S_1} - E_{T_0}$ , the axial value is negative in agreement with the experimental finding that  $D_{x'} < D_{z'}$  (see Table I).

#### D. Interpretation of the $g$ tensor

In this section, we interpret the “rotated” principal axes ( $Y'$ ,  $Z'$ ) of the  $g$  tensor in terms of a slight bending of the Si-H bonds towards one of the silicon dangling bonds. We first assume that the nearly independent dangling bonds  $\varphi_1$  and  $\varphi_2$  are equivalent and that the associated  $g$  tensors are

cylindrical with principal values<sup>24</sup>  $\delta g_{\parallel} = 0$ ,  $\delta g_{\perp} \sim 0.01$ , and with their axes directed along  $[111]$  and  $[\bar{1}\bar{1}1]$ , respectively. In the coordinate system  $(x, y, z)$  of Fig. 7, the  $\delta g$  matrices then are given by

$$\delta \mathbf{g}^{(1)} = \delta g_{\perp}(1) \begin{pmatrix} 1 & 0 & 0 \\ 0 & \frac{1}{3} & -\frac{\sqrt{2}}{3} \\ 0 & -\frac{\sqrt{2}}{3} & \frac{2}{3} \end{pmatrix},$$

$$\delta \mathbf{g}^{(2)} = \delta g_{\perp}(2) \begin{pmatrix} 1 & 0 & 0 \\ 0 & \frac{1}{3} & \frac{\sqrt{2}}{3} \\ 0 & \frac{\sqrt{2}}{3} & \frac{2}{3} \end{pmatrix}, \quad (14)$$

and, hence, the  $\delta g$  matrix of  $VH_2^*$  is [See Eq. (4)]

$$\delta \mathbf{g}^{\text{Theo}} = \frac{1}{2} \begin{pmatrix} \delta g_{\perp}(1) + \delta g_{\perp}(2) & 0 & 0 \\ 0 & \frac{1}{3}(\delta g_{\perp}(1) + \delta g_{\perp}(2)) & \frac{\sqrt{2}}{3}(\delta g_{\perp}(2) - \delta g_{\perp}(1)) \\ 0 & \frac{\sqrt{2}}{3}(\delta g_{\perp}(2) - \delta g_{\perp}(1)) & \frac{2}{3}(\delta g_{\perp}(1) + \delta g_{\perp}(2)) \end{pmatrix}. \quad (15)$$

With  $\delta g_{\perp}(1) = \delta g_{\perp}(2) = \delta g_{\perp}$  this matrix becomes diagonal with the principal values  $\delta g_{\perp}$ ,  $\frac{1}{3}\delta g_{\perp}$ , and  $\frac{2}{3}\delta g_{\perp}$ . It appears from Eq. (15) that off-diagonal elements in  $\delta \mathbf{g}^{\text{Theo}}$  will result if  $\delta g_{\perp}(1)$  and  $\delta g_{\perp}(2)$  become unequal:  $\delta g_{yz}^{\text{Theo}} = \frac{1}{\sqrt{2}}[\delta g_{\perp}(2) - \delta g_{\perp}(1)]$ . In the  $(x, y, z)$  coordinates the experimental  $\delta g$  matrix is

$$\delta \mathbf{g}^{\text{Exp}} = \begin{pmatrix} 0.0117 & 0 & 0 \\ 0 & 0.0043 & 0.0010 \\ 0 & 0.0010 & 0.0062 \end{pmatrix}. \quad (16)$$

Taking the values  $\delta g_{\perp}(1) + \delta g_{\perp}(2) = 0.0222$  and  $\delta g_{\perp}(2) - \delta g_{\perp}(1) = 0.0041$ , we obtain from Eq. (15)

$$\delta \mathbf{g}^{\text{Theo}} = \begin{pmatrix} 0.0111 & 0 & 0 \\ 0 & 0.0037 & 0.0010 \\ 0 & 0.0010 & 0.0074 \end{pmatrix}, \quad (17)$$

in good agreement with Eq. (16).

Within the conventional second-order perturbation treatment,  $\delta g_{\perp}(j)$  ( $j=1,2$ ) may be expressed

$$\delta g_{\perp}(j) \approx \frac{A_{vb}}{E^0(vb) - E_j^0} + \frac{B_{cb}}{E^0(cb) - E_j^0}. \quad (18)$$

Here  $E^0(vb)$  and  $E^0(cb)$  are average one-electron energies in the valence and conduction bands, respectively,  $E_j^0$  is the unperturbed energy of the dangling bond  $\varphi_j$ , and  $A_{vb}$  and  $B_{cb}$  are, apart from a common factor, given as the sums

$$A_{vb} = -2 \sum_{\varphi_n \in VB} \langle \varphi_n | R_x | \varphi_j \rangle \langle \varphi_j | L_x | \varphi_n \rangle, \quad (19a)$$

$$B_{cb} = -2 \sum_{\varphi_m \in CB} \langle \varphi_m | R_x | \varphi_j \rangle \langle \varphi_j | L_x | \varphi_m \rangle, \quad (19b)$$

where  $R_x$  for a single electron is given in Eq. (6).

The first-order effect of a small “external” perturbation that makes  $\varphi_1$  and  $\varphi_2$  inequivalent is a splitting of the degenerate levels  $E_1$  and  $E_2$ , while the electron density residing in  $\varphi_1$  and  $\varphi_2$ , and thus the matrix elements in Eqs. (19a) and (19b), are left unchanged. Hence, the resultant value of  $\delta g_{\perp}(2) - \delta g_{\perp}(1)$  depends in this approximation primarily on the splitting  $E_2 - E_1$ . The parameters in the expression for  $\delta g_{\perp}(j)$  ( $j=1,2$ ) in Eq. (18) are not known with any precision. From the discussion in Ref. 25 it appears, however, that  $A_{vb} \approx 2.7B_{cb}$  and that the average excitation energies  $|E^0(vb) - E_j^0|$  and  $|E^0(cb) - E_j^0|$  are about 1.5 and 2.5 eV, respectively. With these estimates and taking the value  $\delta g_{\perp} = 0.011$  we may obtain a value of  $A_{vb}$ , which in turn suggests that the observed value  $\delta g_{\perp}(2) - \delta g_{\perp}(1) = 0.0041$  cor-

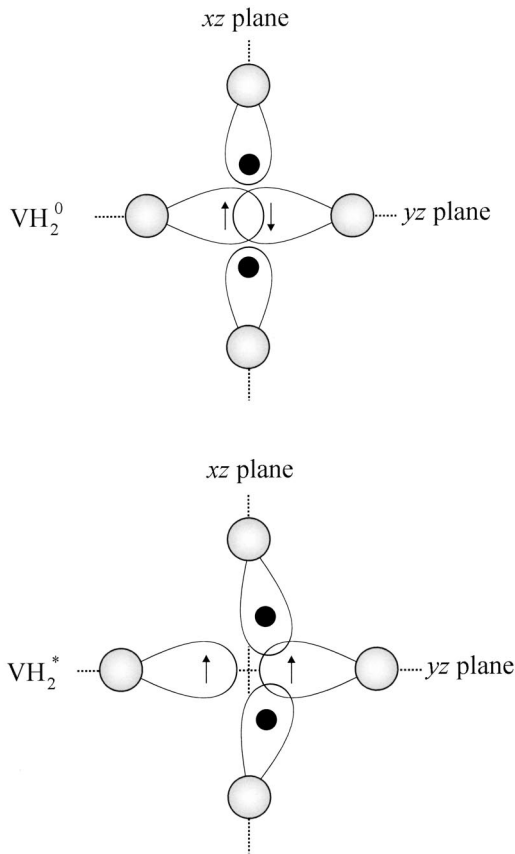


FIG. 8. Molecular models showing the difference between  $VH_2^0$  and  $VH_2^*$ . The defects are viewed along the  $[001]$  axis (the  $z$  axis in Fig. 7). In  $VH_2^0$ , the two silicon atoms in the  $yz$  plane have moved towards the center of the vacancy to form a Si-Si bond. In  $VH_2^*$ , there is no net bonding between these atoms, and one of the free dangling bonds interacts with the two Si-H bonds.

responds to a splitting  $E_2 - E_1 \sim 0.3$  eV. We note that since the electron density in  $\varphi_1$  and  $\varphi_2$  is unchanged to first order in the asymmetric perturbation, so is the  $D$  tensor as calculated within the point-dipole model. Accordingly, the significant, monoclinic- $I$  component of  $\delta g^{\text{Exp}}$  is within this description consistent with the observed almost orthorhombic- $I$   $D$  tensor.

Since the  $D$  tensor indicates that the silicon nuclei bordering the vacancy of  $VH_2^*$  has retained the  $C_{2v}$  geometry of  $VH_2^0$ , we may assume that the perturbation acting on the dangling-bond electrons in  $VH_2^*$  reflects an asymmetric position of the two hydrogen atoms. We propose that one of the singly occupied dangling bonds and the two Si-H bonding orbitals combine to form weak three-electron bonds between the hydrogen atoms and the (distant) silicon atom carrying the dangling bond. Therefore, the Si-H bonds bend somewhat to enhance the electron overlap with the pertinent dangling bond. The proposed distortion is shown schematically in Fig. 8, whereas the mechanism of the three-electron bond is indicated in Fig. 9. By a slight mixing of the Si-H bonding orbital with the dangling-bond orbital, a net stabilization is obtained because the resultant upper level is singly occupied only, while the lower level is doubly occupied. The observa-

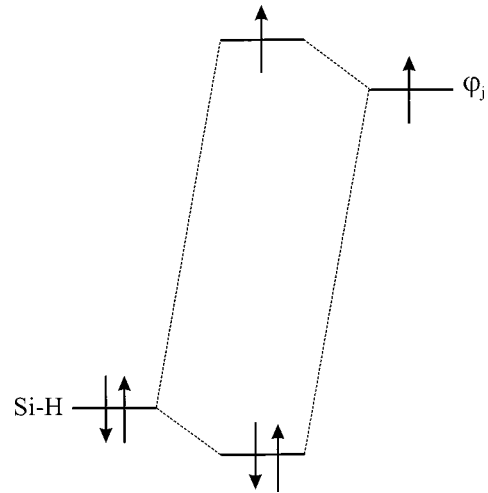


FIG. 9. Schematic representation of the proposed three-electron bond: A slight mixing of the Si-H bonding orbital with the dangling-bond orbital leads to a net stabilization because the bonding combination is doubly occupied whereas the antibonding combination contains only one electron.

tion that  $VH_2^*$  distorts whereas  $VH_2^0$  does not is most simply explained in terms of the “molecular” orbitals  $\varphi_{\pm} = 1/\sqrt{2} \pm 2S_{12}(\varphi_1 \pm \varphi_2)$ . As indicated in Fig. 8, the overlap between  $\varphi_1$  and  $\varphi_2$  in  $VH_2^*$  is small and consequently the splitting between  $\varphi_+$  and  $\varphi_-$  is also small. In a  $C_{2v}$  geometry (orthorhombic- $I$ ) the Si-H bonding orbitals overlap with  $\varphi_+$  only. By distortion to  $C_{1h}$  symmetry (monoclinic- $I$ ), the overlap with  $\varphi_+$  increases and, moreover, an overlap with  $\varphi_-$  now also contributes to the stabilization. In  $VH_2^0$  the overlap between  $\varphi_1$  and  $\varphi_2$  is large, implying a substantial splitting between  $\varphi_+$  and  $\varphi_-$ . In the  $C_{2v}$  geometry an overlap between the Si-H bonds and  $\varphi_+$  does occur, but fails to stabilize the system because  $\varphi_+$  is doubly occupied. Moreover, in this case a distortion to  $C_{1h}$  symmetry, allowing an overlap with the empty  $\varphi_-$ , would probably lead to only a negligible stabilization owing to the high energy of  $\varphi_-$ .

The stabilization of  $VH_2^*$  by the weak three-electron bonds would apparently be the same if the two hydrogen atoms were displaced towards different silicon atoms rather than towards the same silicon atoms as suggested in Fig. 8. However, in that case the resulting configuration would have  $C_2$  symmetry (monoclinic- $II$ ). Since only the  $C_{1h}$  configuration is observed, some subtle interaction between the hydrogen atoms would seem to govern the distortion.

Based on the discussion above, we propose that an interaction between the two hydrogen atoms of  $VH_2^*$  and one of the dangling bonds splits the levels  $E_1$  and  $E_2$  by about 0.3 eV, and thereby accounts for the monoclinic- $I$  component of the  $g$  tensor.

### E. Si-H stretch modes of $VH_2$

If  $VH_2$  is present either in its positive or its negative charge state, the defect is paramagnetic because it then possesses an unpaired electron. Thus, the fact that no EPR signal ascribable to  $VH_2$  is observed when the light is switched off

suggests that the defect is in its neutral charge state,  $\text{VH}_2^0$ , when the sample is not illuminated. Therefore, we assign the Si-H modes of  $\text{VH}_2$  at 2122 and 2145  $\text{cm}^{-1}$  to  $\text{VH}_2^0$ . Previous uniaxial stress experiments<sup>5</sup> have shown that the defect giving rise to the 2122- and 2145- $\text{cm}^{-1}$  modes has orthorhombic- $I$  symmetry in accordance with the discussion in the previous subsection.

The 2122- $\text{cm}^{-1}$  mode is the asymmetric stretch mode<sup>5</sup> for which the dipole moment oscillates along the  $x$  axis ( $[1\bar{1}0]$ ) in Fig. 7, whereas the 2145- $\text{cm}^{-1}$  mode is the symmetric stretch mode with the oscillating dipole moment along the  $z$  axis ( $[001]$ ). As can be seen from Fig. 5, the asymmetric mode is more intense than the symmetric mode, which may be understood qualitatively in a very simple way: The dipole moment induced by the stretching of a Si-H bond will be nearly aligned with the bond. Because the Si-H bonds in  $\text{VH}_2^0$  (Fig. 7) roughly point along the  $[1\bar{1}\bar{1}]$  and the  $[\bar{1}1\bar{1}]$  directions, the component of their oscillating dipole moments is larger along the  $x$  axis than along the  $z$  axis. Since the intensities of the modes are proportional to the square of the oscillating dipole moments, the intensity of the asymmetric stretch mode must therefore exceed that of the symmetric stretch mode. Although the Si-H bonds in  $\text{VH}_2^*$  are somewhat distorted, as discussed in the previous subsection, we expect them to still be roughly aligned with the pertinent  $\langle 111 \rangle$  directions. Based on the relative intensity of the 2063- and the 2077- $\text{cm}^{-1}$  lines, we therefore ascribe them to the asymmetric and the symmetric modes of  $\text{VH}_2^*$ , respectively.

The stretch-mode frequencies of  $\text{VH}_2^*$  are lower than those of  $\text{VH}_2^0$ . Due to the distortion of the Si-H bonds in  $\text{VH}_2^*$  towards one of the silicon atoms carrying a dangling bond, the Si-H bonds in  $\text{VH}_2^*$  will be slightly longer than in  $\text{VH}_2^0$ . Quite generally, a larger bond length  $r_0$  leads to a lower stretch frequency  $\omega_0$ . Morse<sup>26</sup> was among the first to realize this and suggested that  $r_0^3\omega_0$  is nearly a constant. Thus, we get

$$\frac{d\omega_0}{\omega_0} = -3 \frac{dr_0}{r_0}. \quad (20)$$

With the 59- $\text{cm}^{-1}$  difference between the 2122- and 2063- $\text{cm}^{-1}$  modes and assuming that  $r_0$  has the same value as in silane<sup>27</sup> (1.480 Å), we estimate that  $dr_0 \sim 0.014$  Å, i.e., the Si-H bond length in  $\text{VH}_2^*$  is about 0.014-Å longer than that of  $\text{VH}_2^0$ .

The illumination-induced intensity drop of the  $\text{VH}_2^0$  modes in the spectrum shown in Fig. 5(b) is about 5%, which suggests that during steady-state illumination 5% of the neutral  $\text{VH}_2$  complexes are in their excited spin-triplet state ( $\text{VH}_2^*$ ) in this case.

The fact that the isochronal annealing of  $\text{VH}_2^*$  (monitored with the 2063- $\text{cm}^{-1}$  line) differs from that of  $\text{VH}_2^0$  (monitored with the 2122- $\text{cm}^{-1}$  line), as shown in Fig. 6, may be explained as follows: The number of  $\text{VH}_2^*$  defects present during steady-state illumination depends on the lifetime and the number of free carriers, which in turn depend on the number and types of band-gap electronic states. When elec-

trically active defects are removed from the sample by annealing, paths by which the free carriers may recombine disappear, which should increase the steady-state concentration of  $\text{VH}_2^*$ . The  $\text{VH}^0$  and  $\text{V}_n\text{H}^0$  ( $n=3,4$ ) defects, which abound in our samples, decay after heat treatment at  $\sim 470$  and  $\sim 520$  K, respectively.<sup>14</sup> Since these defects are electrically active, their annealing may explain the increase in the number of  $\text{VH}_2^*$  defects above  $\sim 450$  K (see Fig. 6). However, at annealing temperatures above  $\sim 500$  K the total number of  $\text{VH}_2$  defects begins to decrease and the enhanced efficiency of  $\text{VH}_2^*$  formation has to compete with the thermal breakup of  $\text{VH}_2$ . The fraction of  $\text{VH}_2^*$  defects increases from 2% after annealing at 450 K up to 18% after annealing at 575 K. It is uncertain how far this increase goes, but the observation of a relatively strong  $\text{VH}_2^*$  signal after annealing even at 623 K, where the  $\text{VH}_2^0$  signal is very small, suggests that the fraction of  $\text{VH}_2^*$  defects is maximal (well above 18%) just before  $\text{VH}_2$  anneals completely.

### F. Comparison of $\text{VH}_2^*$ with $\text{VO}^*$

Our results reveal, as expected, that the electronic properties of  $\text{VH}_2^*$  and  $\text{VO}^*$  are very similar. Even so, there are important differences between the two defects. First,  $\text{VO}^*$  does not exhibit a distortion from orthorhombic- $I$  symmetry. The overlap between the oxygen lone-pair orbitals and the singly occupied dangling-bond orbitals is at maximum in the  $C_{2v}$  configuration and this counteracts any distortion. Secondly, the separation  $R$  between the two silicon atoms carrying the dangling bonds is shorter in  $\text{VH}_2^*$  than in  $\text{VO}^*$ , as deduced from the  $D$  tensors. Within the point-dipole approximation described above,  $R=4.1$  Å for  $\text{VH}_2^*$  and  $R=4.3$  Å for  $\text{VO}^*$ . This difference is consistent with the expected lattice relaxations around the two defects: The two hydrogen atoms in  $\text{VH}_2^*$  repel each other,<sup>5</sup> which leads to an outwards distortion of the two silicon atoms bonded to hydrogen. Conversely, the oxygen atom in  $\text{VO}^*$  pulls the two silicon atoms bonded to oxygen inwards. Due to the elastic response of the lattice, the distance  $R$  is expected to be smaller in  $\text{VH}_2^*$  than in  $\text{VO}^*$ . Thirdly, the observed signs (phases) of corresponding EPR transitions in the two EPR signals are different for  $\mathbf{B}_0$  along  $[001]$ , as may be seen from Fig. 1. The sign and intensity of a line depend on the population difference between the two levels involved in the EPR transition. The populations of the triplet sublevels are determined by the rates at which these levels become populated as a result of the illumination, and by the rates at which the defect returns to the electronic ground state. Whereas the return to the ground state is governed by the spin-orbit interaction, and is hence spin dependent, the population of the triplet sublevels can both be spin dependent and spin independent: When a  $\text{VH}_2$  defect in the ground state captures a free electron and a free hole created by the band-gap illumination, the defect can end up either directly in one of the excited triplet substates with equal probability or in an excited singlet state, from which it can decay in a spin-dependent way to the triplet substates. Neglecting the spin-dependent generation and using the expressions given by Vlasenko *et al.*<sup>28</sup> for the transi-

tion rates between the ground state and the triplet substrates, it is possible to predict the signs of the EPR lines when  $\mathbf{B}_0$  is along one of the principal axes of the  $D$  tensor. These predictions are consistent with the observed signs of the corresponding  $\text{VO}^*$  lines, but not with those observed for  $\text{VH}_2^*$ , which may be taken to suggest that spin-dependent generation of  $\text{VH}_2^*$  may be important.

## V. SUMMARY

The effect of band-gap illumination on the EPR spectra of proton- and deuteron-implanted silicon has been measured. An EPR signal  $DK5$ , which originates from an excited spin-triplet state of a defect with monoclinic- $I$  (near-orthorhombic- $I$ ) symmetry, is observed. The similarity of the  $D$  tensor of  $DK5$  with that of  $\text{VO}^*$  indicates that the two unpaired electrons in the  $DK5$  defect reside primarily at two silicon sites adjacent to a monovacancy. The intensity of  $DK5$  is identical in the spectra of float-zone and Czochralski-grown samples, indicating that the underlying defect does not contain oxygen. The observed, partially resolved anisotropic hyperfine splittings are consistent with the expected proton hyperfine splittings of  $\text{VH}_2^*$ .

Combining these observations we assign the  $DK5$  signal to the defect  $\text{VH}_2^*$ . It is interesting to note that the excitation of  $\text{VH}_2^0$  from the electronic ground state to the excited spin-

triplet state leads to a small distortion, changing the symmetry from orthorhombic- $I$  to monoclinic- $I$ . A similar distortion does not occur for  $\text{VO}^*$ . This indicates that the presence of the electronically nearly inert units Si-O-Si in  $\text{VO}^*$  and Si-H in  $\text{VH}_2^*$  do have an observable effect on the electronic properties of these defects. Still, the electronic properties of  $\text{VH}_2^*$  and  $\text{VO}^*$  are similar as expected, being dominated by the populations of the bonding and antibonding combinations of the two broken silicon orbitals that are not satisfied by hydrogen or oxygen.

From parallel isochronal annealings monitored with EPR and FTIR it is concluded that  $\text{VH}_2^*$  possesses Si-H stretch modes at 2063.1 and 2077.4  $\text{cm}^{-1}$ . Based on their relative intensities, the 2063.1- and 2077.4- $\text{cm}^{-1}$  modes are identified as the asymmetric and the symmetric stretch modes, respectively. The fraction of  $\text{VH}_2^0$  defects present as  $\text{VH}_2^*$  during illumination is estimated to be  $\sim 2\%$  for the as-prepared samples. This percentage increases rapidly with annealing temperature, but at  $\sim 590$  K the  $\text{VH}_2^*$  signals disappear due to thermal decay of  $\text{VH}_2$ .

## ACKNOWLEDGMENT

This work was supported by the Danish National Research Foundation through the Aarhus Center for Atomic Physics (ACAP).

\*Author to whom correspondence should be addressed. Electronic address: bbn@phys.au.dk

<sup>1</sup>See *Hydrogen in Semiconductors, Semiconductors and Semimetals*, edited by J. I. Pankove and N. M. Johnson (Academic, San Diego, 1991), Vol. 34, and references therein.

<sup>2</sup>See S. J. Pearton, J. W. Corbett, and M. Stavola, *Hydrogen in Crystalline Semiconductors* (Springer-Verlag, Berlin, 1992), and references therein.

<sup>3</sup>See *Hydrogen in Semiconductors II, Semiconductors and Semimetals*, edited by N. M. Nickel (Academic, San Diego, 1999), Vol. 61, and references therein.

<sup>4</sup>B. Bech Nielsen, L. Hoffmann, and M. Budde, *Mater. Sci. Eng.*, **B 36**, 259 (1996).

<sup>5</sup>B. Bech Nielsen, L. Hoffmann, M. Budde, R. Jones, J. Goss, and S. Öberg, in *Defects in Semiconductors 18, Materials Science Forum*, edited by M. Suezawa and H. Katayama-Yoshida (Trans-Tech, Zürich, 1995), Vols. 196–201, p. 933.

<sup>6</sup>B. Bech Nielsen, P. Johannesen, P. Stallinga, K. Bonde Nielsen, and J. R. Byberg, *Phys. Rev. Lett.* **79**, 1507 (1997).

<sup>7</sup>T. L. Cottrell, *The Strengths of Chemical Bonds* (Butterworth, Washington, DC, 1954), p. 273.

<sup>8</sup>G. D. Watkins and J. W. Corbett, *Phys. Rev. A* **134**, A1359 (1964).

<sup>9</sup>G. D. Watkins and J. W. Corbett, *Phys. Rev.* **121**, 1001 (1961).

<sup>10</sup>K. L. Brower, *Phys. Rev. B* **4**, 1968 (1971); *Radiat. Eff.* **8**, 213 (1971).

<sup>11</sup>W. M. Chen, O. O. Awadelkarim, B. Monemar, J. L. Lindström, and G. S. Oehrlein, *Phys. Rev. Lett.* **64**, 3042 (1990).

<sup>12</sup>P. Stallinga and B. Bech Nielsen, *Phys. Rev. Lett.* **80**, 422 (1998).

<sup>13</sup>W. M. Chen, O. O. Awadelkarim, B. Monemar, J. L. Lindström, and G. S. Oehrlein, *Phys. Rev. Lett.* **80**, 423 (1998).

<sup>14</sup>P. Stallinga, P. Johannesen, S. Herström, K. Bonde Nielsen, B. Bech Nielsen, and J. R. Byberg, *Phys. Rev. B* **58**, 3842 (1998).

<sup>15</sup>A quartet would yield three equidistant fine-structure lines for each distinct orientation, of which the central line would be completely obscured by the very strong  $S=\frac{1}{2}$  signals in the present spectra.

<sup>16</sup>G. V. H. Wilson, *J. Appl. Phys.* **34**, 3276 (1963).

<sup>17</sup>M. Suezawa, *Phys. Rev. B* **63**, 035201 (2000).

<sup>18</sup>M. Budde, G. Lüpke, E. Chen, X. Zhang, N. H. Tolk, L. C. Feldman, E. Tarhan, A. K. Ramdas, and M. Stavola, *Phys. Rev. Lett.* **87**, 145501 (2001).

<sup>19</sup>J. R. Byberg, N. Bjerre, A. Lund, and P.-O. Samskog, *J. Chem. Phys.* **78**, 5413 (1983).

<sup>20</sup>For a general discussion the reader is referred to A. Abragam and B. Bleaney, *Electron Paramagnetic Resonance of Transition Ions* (Dover, New York, 1986), Chap. 9.

<sup>21</sup>T. Moriya, *Phys. Rev.* **120**, 91 (1960).

<sup>22</sup>See, e.g., M. Weissbluth, *Atoms and Molecules* (Academic, New York, 1978), p. 337.

<sup>23</sup>M. H. L. Pryce, *Proc. Phys. Soc., London, Sect. A* **63**, 25 (1950).

<sup>24</sup>E. G. Sieverts, *Phys. Status Solidi B* **120**, 11 (1983).

<sup>25</sup>J. C. Phillips, *Comments Solid State Phys.* **3**, 67 (1970).

<sup>26</sup>P. M. Morse, *Phys. Rev.* **34**, 57 (1929).

<sup>27</sup>*American Institute of Physics Handbook*, edited by D. E. Gray (McGraw-Hill, New York, 1972), pp. 7–196.

<sup>28</sup>L. S. Vlasenko, Yu. V. Martynov, T. Gregorkiewicz, and C. A. J. Ammerlaan, *Phys. Rev. B* **52**, 1144 (1995).